minerals

MDPI

Article

The Genetic Link between Iron-Oxide–Apatite and Porphyry Cu–Au Mineralization: Insight from the Biotite–Pyroxene–Zircon Study of the Nihe Fe Deposit and the Shaxi Cu–Au Deposit in the Lower Yangtze Valley, SE China

Yi Li [1,2], Ke-Zhang Qin [1,2,*], Guo-Xue Song [2], Yu Fan [3], Fang-Yue Wang [3] and Le Wang [1,2]

[1] Key Laboratory of Mineral Resources, Institute of Geology and Geophysics, Chinese Academy of Sciences, Beijing 100029, China
[2] College of Earth and Planetary Sciences, University of Chinese Academy of Sciences, Beijing 101408, China
[3] School of Resources and Environmental Engineering, Hefei University of Technology, Hefei 230009, China
* Correspondence: kzq@mail.iggcas.ac.cn

Abstract: Different ore deposit types may evolve from a common magmatic-hydrothermal system. Establishing a genetic link between different deposit types in an ore cluster can not only deepen the understanding of the magmatic-hydrothermal mineralization process but can also guide exploration. Both the Nihe iron-oxide–apatite (IOA) deposit and the Shaxi porphyry Cu–Au deposit in the Lower Yangtze Valley, Anhui, Southeast China, formed in the Luzong Cretaceous volcanic basin at ~130 Ma. We examined a temporal–spatial and potential genetic link between these deposits based on stratigraphic lithofacies sections, biotite and clinopyroxene mineralogical chemistry, zircon chronology, Hf isotopes, and trace elements. Stratigraphy, petrology, mineralogical chemistry, and available fluid inclusion results support that the emplacement depth of the Nihe ore-related porphyry is shallower than that of the Shaxi porphyry. The magmatic zircon and hydrothermal zircon from Nihe provided U–Pb ages of 130.6 ± 0.7 Ma and 130.7 ± 0.7 Ma, respectively. The magmatic zircon U–Pb age (130.0 ± 0.8 Ma) of Shaxi overlaps with its molybdenite Re–Os age (130.0 ± 1.0 Ma). The agreement between the mineralization and porphyry emplacement ages of Nihe and Shaxi indicates a temporal coincidence and supports a possible genetic link between the two deposits, considering their close spatial relationship (in the same ore district, 15 km). The zircon Hf isotopes and trace elements support the evolution of both deposits from an enriched lithospheric mantle, although the Shaxi deposit may have experienced contamination of the Jiangnan-type basement. Both deposits lie above the fayalite-magnetite-quartz buffer, but the Nihe magmatic zircons are of lower temperature and less oxidized than that of Shaxi. The much higher Eu/Eu* and Yb/Dy values of zircons from Shaxi are likely caused by the suppression of early plagioclase crystallization and the prevalence of amphibole fractionation, thus indicating more hydrous content of the Shaxi ore-related magma. Additionally, the Shaxi ore-related porphyry has higher zircon Hf concentrations, suggesting that the porphyry Cu–Au deposit has experienced a greater degree of magma fractionation. Our study highlights that the Nihe IOA deposit and the Shaxi porphyry Cu–Au deposit have a common magma source, while different extent of crust contamination, magma oxidation state, hydrous content, and degree of magma fractionation collectively result in the two distinct ore deposits. This possible genetic link suggests a great potential of porphyry Cu–Au-PGE mineralization in the Middle–Lower Yangtze River metallogenetic belt, especially in the deep part of the IOA district in the Luzong Cretaceous volcanic basin.

Keywords: magmatic-hydrothermal system; Nihe IOA deposit; Shaxi porphyry Cu–Au deposit; biotite–clinopyroxene–zircon mineralogy; temporal–spatial and genetic link

1. Introduction

Magmatism provides a heat source, metal, and ore-forming fluid for many magmatic-hydrothermal deposits [1,2]. Different deposit types can be developed in a common magmatic-hydrothermal system due to different temperatures, pressures, and wall rock properties [2]. For example, skarn Cu–Au, carbonate-replacement Zn–Pb–Ag–Au, and distal sedimentary Au deposits successively developed around the Bingham porphyry Cu–Au–Mo deposit in the USA [2,3]. In Southeast China, the skarn Fe and magmatic-hydrothermal Cu–Au deposits have been discovered around the IOA deposits in Luzong, Ningwu, and Jinniu volcanic basins [4–6]. As such, research on the temporal–spatial and genetic relationship between different deposit types in an ore district plays a crucial role in understanding the magmatic-hydrothermal evolution processes and aiding exploration.

The Middle–Lower Yangtze River metallogenetic belt (MLYRMB) has been well known for the late-Jurassic to early Cretaceous skarn-porphyry Fe–Cu–Au–Mo–W mineralization (151–135 Ma) since the 1970s (Figure 1A; [7–12]). A series of alkalic porphyry Cu–Au deposits and occurrences had been found in the Cretaceous volcanic basin at Luzong, Ningwu in the Lower Yangtze Valley, with large-scale IOA deposits (133–125 Ma) (Figure 1A,B; [8,13–16]). In particular, the Shaxi porphyry Cu–Au deposit in the north of the Luzong Cretaceous volcanic basin is temporally and spatially associated with the Nihe IOA deposit (Figure 1A,B; [17–19]), which provides a good example for studying the genetic relationship between IOA and porphyry Cu–Au mineralization.

Zircon is a common accessory mineral in magmatic intrusion which has stable physical and chemical characteristics and can retain a magma nature during and after zircon crystallization [20,21]. Thus, zircon can provide not only the age of crystallization, but also information on the magma source, oxygen fugacity, and water content of the ore-forming magma [20,22–26]. In addition, clinopyroxene provides information on the crystallization temperature and pressure in sub-alkaline basic to intermediate magmas [27,28]. The total Al content of biotite increases with increasing pressure [29], while the Ti content of biotite decreases with increasing Mg/(Mg + Fe) values under a given temperature [30]. Thus, the P–T conditions of ore-forming magma can be constructed using these minerals.

In this paper, we examine a genetic link between the Nihe IOA and the Shaxi porphyry Cu–Au mineralization by integrating zircon U–Pb dating, Hf isotopes, trace elements, and major elements of clinopyroxene and biotite. We suggest that such a link would provide useful guidance for future porphyry Cu–Au-PGE exploration in the Lower Yangtze Valley and other areas that contain IOA deposits in similar tectonic settings.
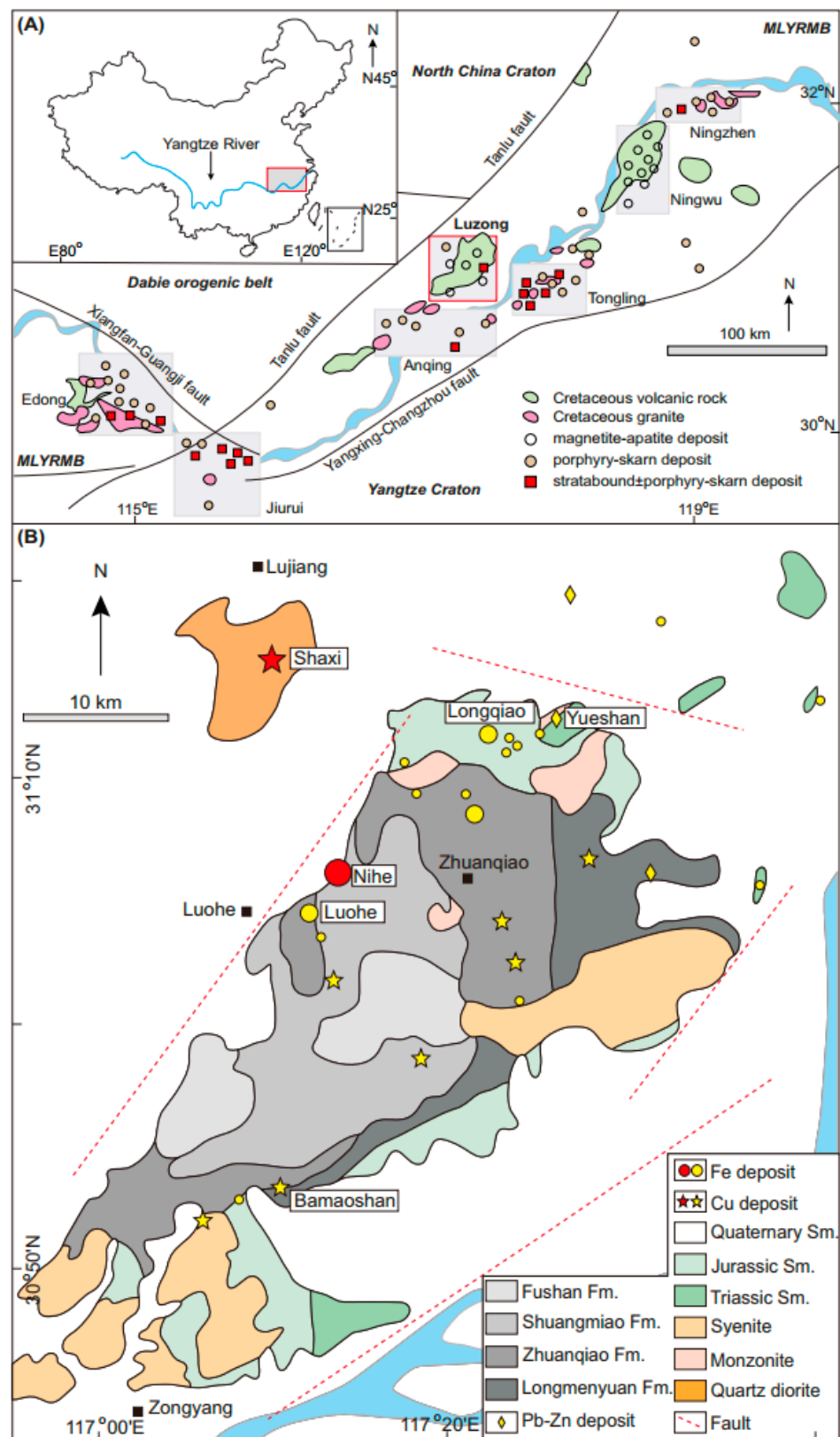
Figure 1. (**A**) Distribution of the major Cretaceous igneous rocks and mineral deposits in the Middle–Lower Yangtze River metallogenic belt, South China. The map is modified after Li et al. [31]. (**B**) Distribution of Fe, Cu, and Pb–Zn deposits including IOA (Nihe) and porphyry Cu–Au (Shaxi) in the Luzong basin modified after [17]. Abbreviations: Fm. = Formation; Sm. = Sedimentary.

2. Geological Setting

The MLYRMB, located in the northeast of the Yangtze Craton, southeastern China, is one of the most important Cu–Fe–Au–Mo–W polymetallic metallogenic belts in China (Figure 1A; [7–10]). It consists of seven ore districts from west to east: Edong, Jiurui, Anqing-Guichi, Luzong, Tongling, Ningwu, and Ningzhen (Figure 1A). Among them, Edong, Jiurui, Anqing-Guichi, Tongling, and Ningzhen are characterized by the presence of porphyry-skarn Cu–Fe–Au–Mo deposits related to high-K calc-alkaline granitoids, whereas the Lower Yangtze Valley (especially in the Luzong and Ningwu Cretaceous volcanic basin) is characterized by IOA deposits related to shoshonite and/or high-K calc-alkaline volcanic–subvolcanic rocks (Figure 1A; [19,32]). There are three epochs of porphyry mineralization at the MLYRMB: the early (151–135 Ma) and late (123–105 Ma) stages are composed of porphyry-skarn mineralization, while the middle stage (133–125 Ma; the same period as IOA deposits) is composed of porphyry Cu–Au mineralization [19,31,33,34]. However, only one porphyry deposit (Shaxi Cu–Au deposit; Figure 1B) has been discovered in the MLYRMB as the middle stage of porphyry Cu–Au mineralization. Since porphyry deposits are characterized by linear clusters and 10–20 Ma periodic mineralization, e.g., deposits at the Andes, South America; Gangdese, Tibet [35,36], there is thus great exploration potential for porphyry Cu–Au deposits (between 133–125 Ma) in this area [11,19,37,38].

In the Luzong basin, Lower Yangtze Valley, the earliest sedimentary rocks are the Silurian strata, which consists of beach-lagoon facies clastic rocks and is the main wall rock of the Shaxi porphyry Cu–Au deposit [16]. The Silurian sedimentary rocks are overlain by the Triassic marine-evaporation platform sedimentary rocks, including siltstone, limestone, Ca-dolomite, mudstone, as well as some anhydrite, hematite, and siderite layers [16,18]. The Jurassic continental clastic rocks rest on the Triassic strata, primarily consisting of arkose sandstone, shale, and siltstone [16,39]. Subsequently, the extensive and intensive Yanshanian tectonic–magmatic event formed large-scale Cretaceous volcanic rocks in the MLYRMB. In the Luzong Cretaceous volcanic basin, the Cretaceous volcanic rock strata consist of the Longmenyuan Formation, the Zhuanqiao Formation, the Shuangmiao Formation, and the Fushan Formation with zircon U–Pb ages of 134.8 ± 1.8 Ma, 134.1 ± 1.6 M, 130.5 ± 0.8 Ma, and 127.1 ± 1.2 Ma, respectively [40]. Many subvolcanic rocks (131–127 Ma) intruded into the Zhuanqiao Formation [32,41].

3. Geology of Ore Deposits

3.1. The Nihe IOA Deposit

The Nihe IOA deposit, located northwest of the Luzong Cretaceous volcanic basin, Lower Yangtze Valley, is a representative IOA deposit in the MLYRMB (Figures 1 and 2). This deposit contains a reserve of 16.8 Mt Fe, 1.4 Mt anhydrite, and 6.1 Mt pyrite [42]. The layered or lenticular main ore body, with 816 m in length and 445 m in width, is located at the top of the diorite porphyry at a depth of 642–1000 m (Figure 2; [42,43]). Some pyrite orebodies coexist with the magnetite main orebody, while other pyrite orebodies have been discovered in the Zhuanqiao Formation (Figure 2; [44]). Hydrothermal alteration at Nihe is divided into the Lower light-colored zone (alkali feldspar–pyroxene–anhydrite–plagioclase), the Middle dark-colored zone (magnetite–apatite–pyroxene–anhydrite–garnet–chlorite), and the Upper light-colored zone (kaolinite–quartz–sericite–anhydrite) from bottom to top (Figure 2; [43]). Mineralization can be mainly divided into three stages: the early stage is composed of pyroxene/garnet–magnetite ± apatite ± anhydrite; the main stage is composed of magnetite–apatite ± pyrite ± anhydrite; and the late stage is composed of pyrite–anhydrite [13,14].
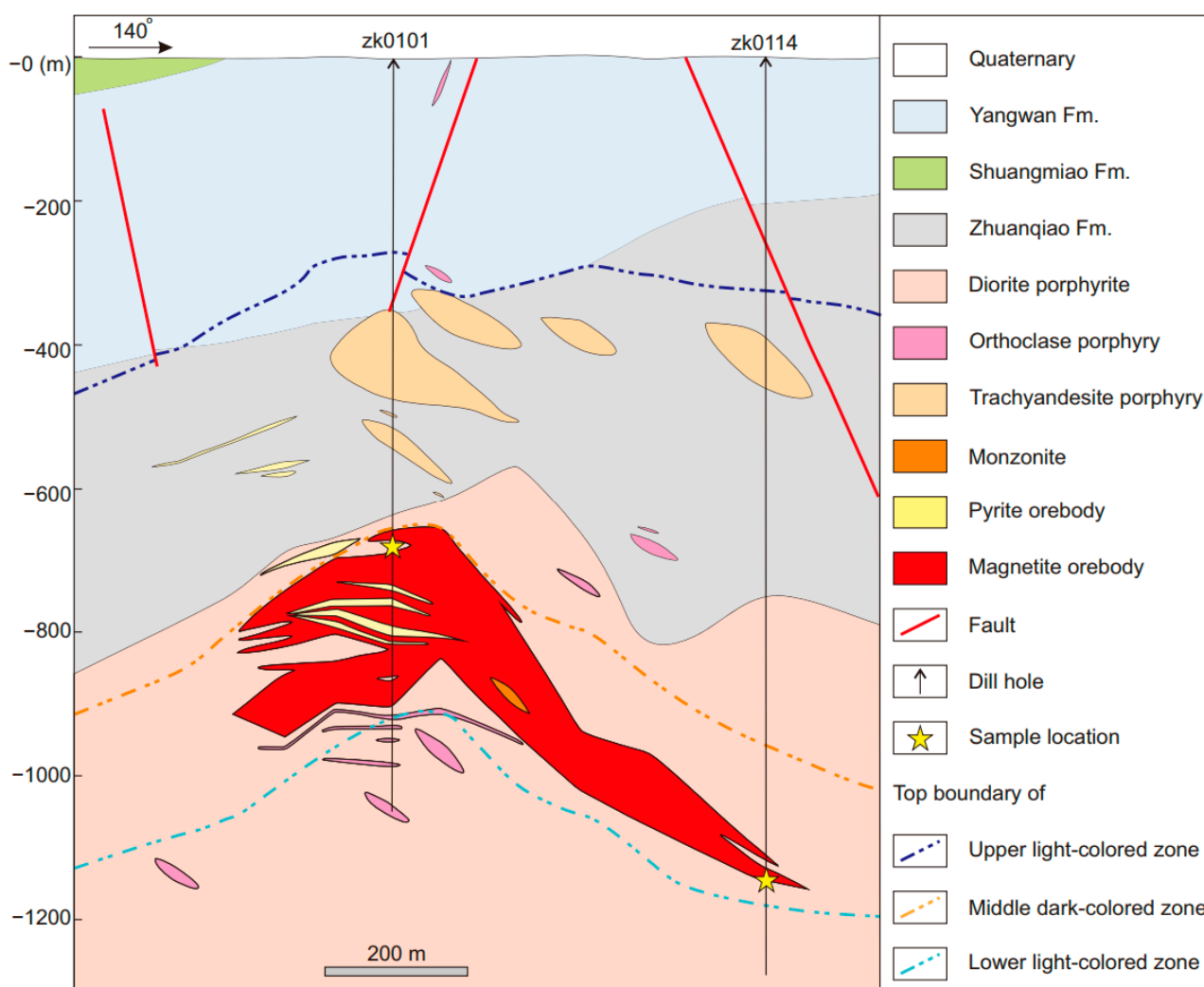
Figure 2. Geological map of Nihe IOA deposit (modified after [43]). Abbreviations: F.m = Formation.

3.2. Shaxi Porphyry Cu–Au Deposit

The Shaxi porphyry Cu–Au deposit, located ~15 km north of the Nihe IOA deposit (Figure 1), is the only reported porphyry deposit formed in the middle stage porphyry mineralization at the MLYRMB so far [19]. The deposit contains a reserve of over 1 Mt Cu and 45 t Au, which is located at the depth of 400–830 m with 884 m in length and 49–483 m in width (Figure 3; [18,45]). The orebody with 15°–35° in trend and 40°–60° in inclination, mainly developed in quartz diorite porphyry, is irregularly lenticular and locally lamellar in profile. The alteration at Shaxi has obvious zones, including potassic alteration (K–feldspar–biotite–magnetite–anhydrite ± quartz), propylitic alteration (chlorite–epidote ± albite ± illite ± calcite ± anhydrite), phyllic alteration (sericite–anhydrite–calcite), and argillic alteration (kaolinite–clay minerals) [18]. The propylitic alteration is often superimposed by phyllic alteration (Figure 3; [45]). Mineralization consists of three stages: the potassic stage, with the occurrence of K–feldspar–biotite–magnetite–quartz–anhydrite ± pyrite ± chalcopyrite; the quartz sulfide stage, which is the main mineralization stage, character-ized by chalcopyrite–quartz–chlorite–epidote–pyrite; and the late quartz–carbonate stage containing quartz–carbonate–anhydrite–clay mineral ± chalcopyrite [18,19,45].
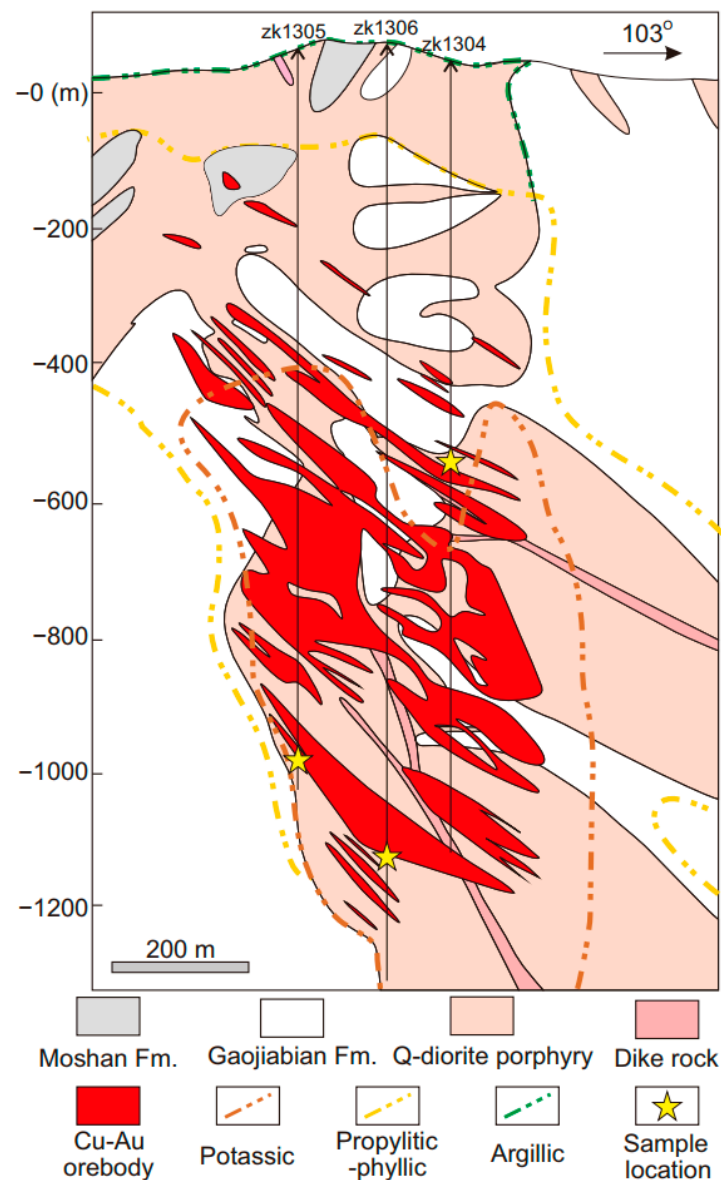
Figure 3. Geological map of the Shaxi porphyry deposit (modified after [45]). Abbreviations: Fm. = Formation.

4. Samples and Analytical Methods

4.1. Samples

Two diorite porphyry samples with disseminated-veined magnetite and veined-spotted magnetite were collected from drill cores ZK0114-1130 and ZK0101-667 (Figures 2 and 4A–F) at Nihe. At Shaxi, three quartz diorite porphyry samples with veined-disseminated chalcopyrite–magnetite–pyrite were collected from drill cores ZK1306-1128, ZK1305-979, and ZK1304-518 (Figures 3 and 5A–F). Zircons from the samples mentioned above were separated by standard density and magnetic separation techniques, and representative zircon grains were mounted in epoxy resin. To select the best location for further analysis, zircon was photographed by the transmitted and reflected light at the Institute of Geology and Geophysics, Chinese Academy of Sciences, and zircon cathodoluminescence (CL) images were taken at the Wuhan SampleSolution Analytical Technology Co., Ltd., (Wuhan, China), Hubei in China (Wuhan SampleSolution).
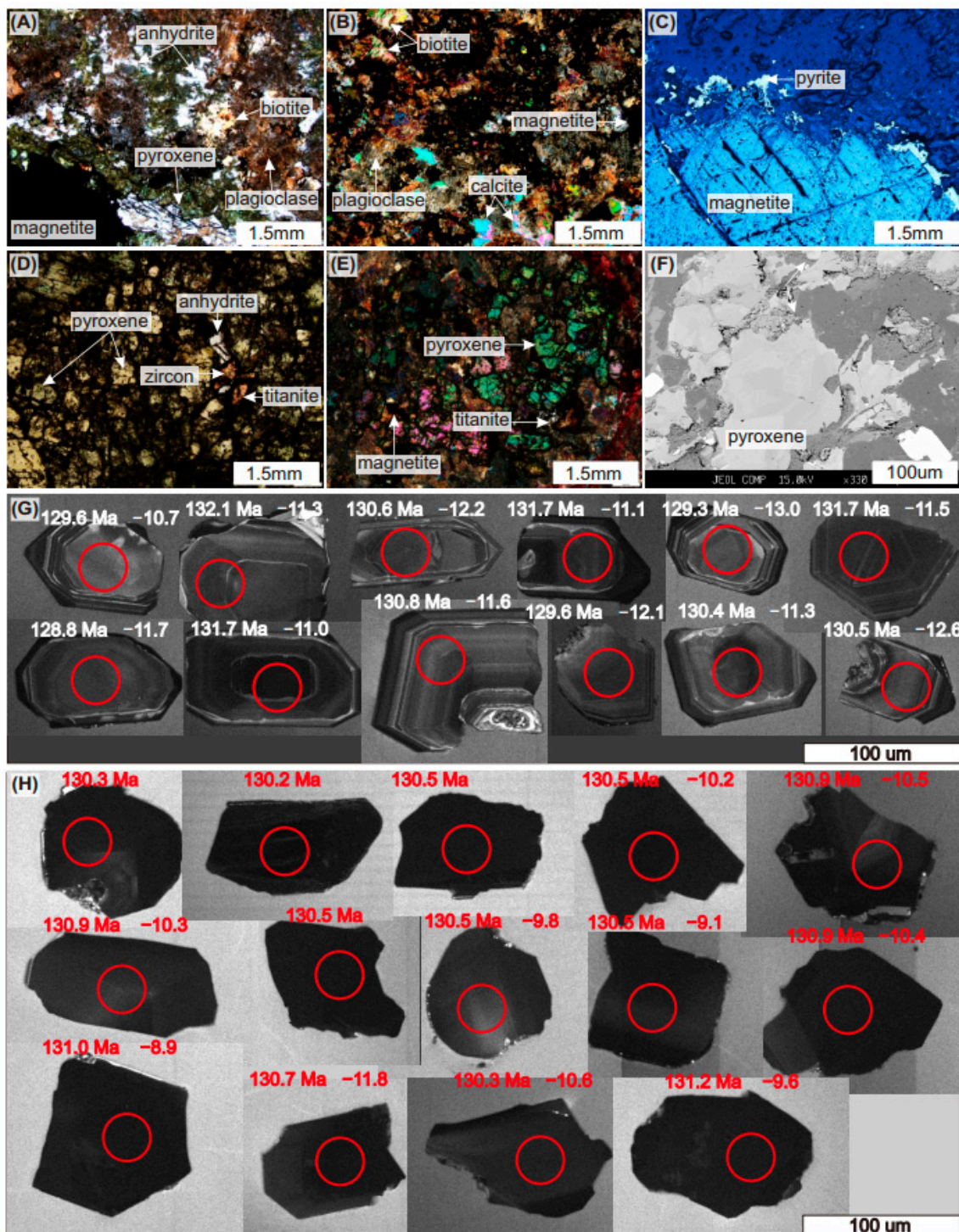
Figure 4. Representative photomicrographs and zircon characteristics of diorite porphyry from the Nihe IOA deposit. The phenocrysts in the diorite porphyry are mainly plagioclase, pyroxene, and biotite (**A**,**B**), and they are closely associated with magnetite. Some pyrite develops around and/or cuts the magnetite (**C**). Zircon occurs in the titanite that is spatially associated with anhydrite (**D**), suggesting that zircon and titanite are of hydrothermal origins. Clinopyroxene is the most important gangue mineral at Nihe (**D**,**E**), and the clinopyroxene has approximate zones in BSE images (**F**). Zircons from ZK0114-1130 have prominent oscillatory zones (**G**), while zircons from ZK0101-667 show inconspicuous oscillatory zones and core-rim structures (**H**). The U–Pb ages and $\varepsilon_{Hf}(t)$ values of these zircons are shown in panels **G** and **H**.
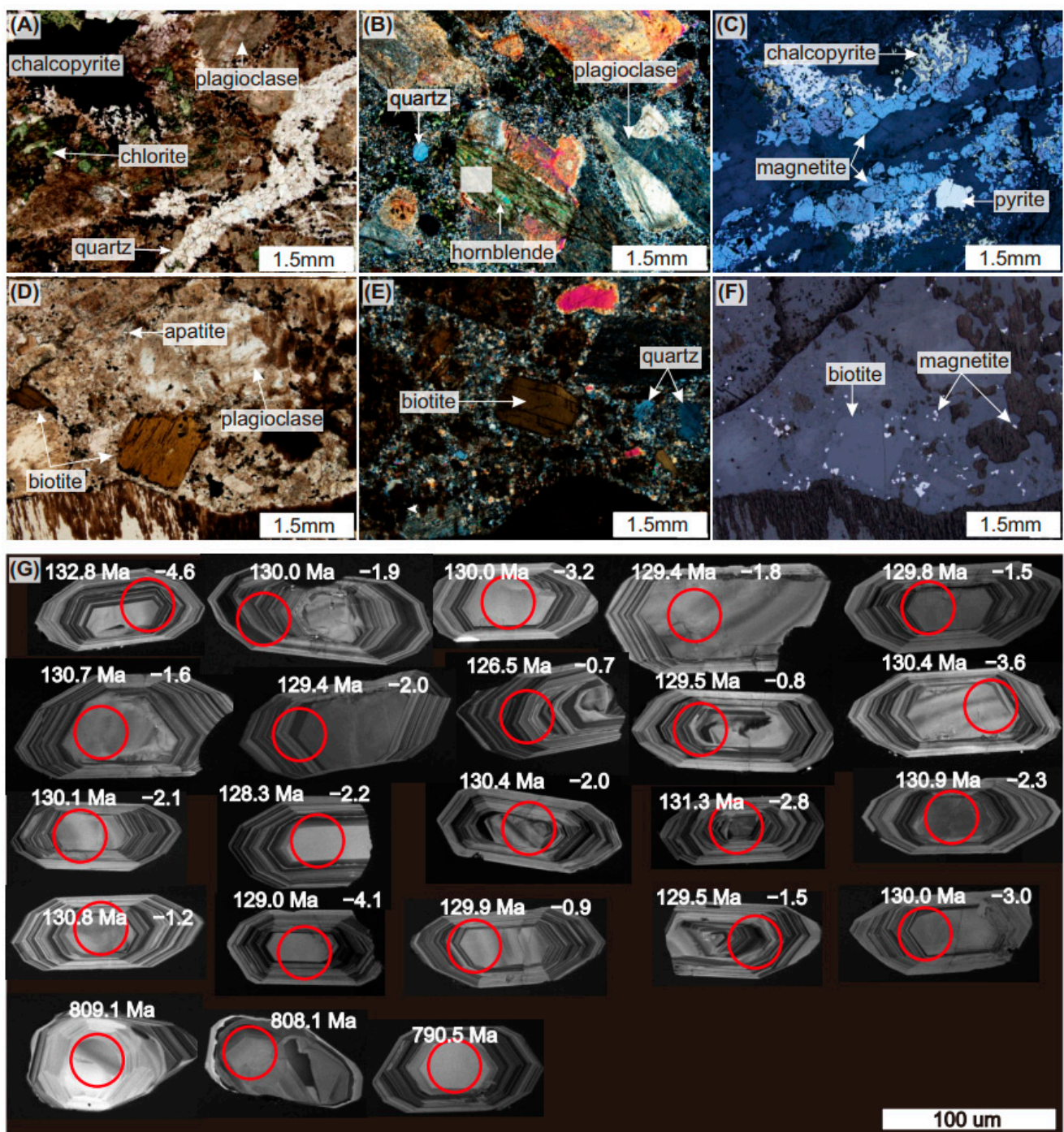
Figure 5. Representative photomicrographs and zircon characteristics of quartz diorite porphyry from Shaxi porphyry Cu–Au deposit. The phenocrysts in the quartz diorite porphyry are mainly plagioclase, hornblende, biotite, and quartz (**A**,**B**,**D**,**E**), and they are closely associated with chalcopyrite and magnetite (**C**,**F**). Biotites are mostly euhedral crystals and show the characteristic of magmatic biotite (**D**–**F**). Zircons from Shaxi have prominent oscillatory zones (**G**), and the U–Pb ages and $\varepsilon_{Hf}(t)$ values of these zircons are shown in panel **G**.

4.2. In Situ Electron Probe Microanalysis of Biotite and Clinopyroxene

Clinopyroxene from Nihe and biotite from Shaxi were identified using the microscope. Unaltered crystals were selected for EPMA using JXA-8230 of JEOL at the Institute of Geology, Chinese Academy of Geological Sciences. The voltage and current analyzed were

15 kV and 10 nA, respectively, and the beam diameter was set at 5 μm. The data correction method adopted the ZAF correction method of JEOL.

4.3. Zircon U–Pb Dating and Trace Element Analysis

In situ zircon U–Pb dating was performed using an Agilent 7900 ICP-MS coupled with an ArF 193 nm excimer laser ablation system (Geolas Pro) at Wuhan SampleSolution. The details of the measurement procedures and data reduction were the same as described previously [46]. A brief summary is provided in the following section.

During the LA-ICPMS analysis, spot sizes were 32 μm, employed with a 5 Hz frequency. Helium and argon were used as the carrier gas and compensation gas, respectively, to improve the signal sensitivity. The zircon standard 91500, Plešovice, and GJ-1 were used as external standards for U–Pb dating. After every 6 test samples, two standard samples were measured for calibration to ensure the reliability of the measured results. Each time-resolved analysis data includes about 20–30 s blank signal and 50 s sample signal. The ICPMSDataCal software [46] was used to complete off-line data reduction. The Concordia U–Pb age diagrams were plotted using Isoplot R [47].

Zircon trace elements were determined by the same LA-ICP-MS system at Wuhan SampleSolution. Analyses were carried out on the zircon grains, whose ages were previously constrained by the U–Pb dating. The details of the measurement procedures and data reduction were the same as mentioned above [46]. Glass standard samples NIST610, BCR-2G, BIR-1G, and BHVO-2G were used as multiple external standards to quantitatively calculate the content of trace elements [46].

4.4. Zircon Hf Isotope Analysis

Zircon Hf isotope analysis was conducted by a Neptune (Plus) MC-ICP-MS (ThermoFisher Scientifc, Bermen, Germany) combined with a Geolas HD excimer ArFlaser ablation system (Coherent, Gottingen, Germany) at the Wuhan SampleSolution. The details of the measurement condition and data reduction were the same as described previously [48]. Hence, only a brief description is given below.

Helium was used as the carrier gas, and a small amount of nitrogen was introduced to improve the sensitivity of Hf isotopes. The laser diameter was set at 32 μm, employed with a 5 Hz frequency. The zircon standard 91500, Plešovice, and GJ-1 were used as external standards for the Hf isotope analysis. The mass bias of Hf (β_{Hf}) and Yb (β_{Yb}) of the zircons was calculated by the $^{179}Hf/^{177}Hf = 0.7325$ and $^{173}Yb/^{171}Yb = 1.132685$ [49] in real-time. The values $^{176}Yb/^{173}Yb = 0.79639$ [49] and $^{176}Lu/^{175}Lu = 0.02656$ [50] were used to correct the interference of ^{176}Yb on ^{176}Hf and ^{176}Lu on ^{176}Hf. The mass fractionation of Lu was calculated by the mass bias of Yb (β_{Yb}). Off-line data reduction was performed by the ICPMSDataCal software [46].

5. Results

5.1. Nihe IOA Deposit

Clinopyroxene is the most important gangue mineral at Nihe, and it was cut or replaced by plagioclase, anhydrite, apatite, magnetite, and titanite (Figure 4A,B,D,E), indicating that it is an early crystallized mineral in the magma system. The backscattered electron (BSE) images of clinopyroxene crystals from Nihe show approximate zones (Figure 4F), indicating that the clinopyroxene formed in a process of decreasing pressure and, accordingly, in the emplacement of the magma. Thus, the rim of the clinopyroxene crystal can record the P–T condition of the ore-forming magma. The SiO_2, TiO_2, Al_2O_3, FeO, MnO, MgO, CaO, and Na_2O of five clinopyroxene crystals rims are 48.93–51.88, 0–0.37, 1.32–2.64, 7.6–14.89, 0.33–0.75, 8.51–13.34, 23.16–24.25, and 0.47–0.63 wt.%, respectively (Table S1). In addition, they produce a temperature and pressure of Nihe of 1038–1121 °C and 39.3–88.9 MPa, respectively, based on clinopyroxene-only thermobarometry (Table S1; [28]).

The CL images of zircons from ZK0114-1130 show prominent oscillatory zones (Figure 4G), and these zircons have Th and U contents of 2371–14,608 ppm and 2310–8476 ppm, re-

spectively, with Th/U values mostly between 0.9 to 1.8 (Table S2), which are similar to magmatic zircon [51]. Zircons from ZK0101-667 show inconspicuous oscillatory zones and core-rim structures (Figure 4H), which have Th and U contents of 3587–67,911 ppm and 4335–33,015 ppm, respectively, and Th/U values of 0.8–3.3 (Table S2). The CL image characteristic and high Th content and Th/U ratios indicate that they have the characteristics of hydrothermal zircons [52], which is supported by the REE characteristics (obvious ΣREE-enrich and negative Eu anomaly; Figure 6A; Table S3). Thus, we suggest that the zircons from ZK0114-1130 and ZK0101-667 are magmatic zircons and hydrothermal zircons, respectively. Twelve magmatic zircon and 14 hydrothermal zircon grains give the concordia age of 130.6 ± 0.7 Ma (MSWD = 6.8; Figure 7A; Table S2) and 130.7 ± 0.7 Ma (MSWD = 11; Figure 7B; Table S2). The average crystallization temperatures of magmatic zircons and hydrothermal zircons are calculated at 657 °C and 951 °C, respectively (Figure 8A–C; Table S3) by a zircon Ti thermometer [53]. The average oxygen fugacity (f_{O2}) of magmatic zircons and hydrothermal zircons is calculated at −17.66 and −11.84, respectively, while their ΔFMQ (the different with fayalite-magnetite-quartz buffer) are 0.99 and 0.06, based on the zircon f_{O2} equation (Figure 8B–D; Table S3; [54]).

For the magmatic zircons from Nihe, their $n(^{176}Lu)/n(^{177}Hf)$ and $n(^{176}Hf)/n(^{177}Hf)$ ratios fall within a range of 0.000231–0.002183 and 0.282366–0.282397 (Table S4). Their $\varepsilon_{Hf}(t)$ values range from −11.6 to −10.5 (mean = −11.1) with a T_{DM1} age of 1210–1277 Ma and T_{DM2} age of 1635–1697 Ma (Figure 9A; Table S4). For the hydrothermal zircons, their $n(^{176}Lu)/n(^{177}Hf)$ and $n(^{176}Hf)/n(^{177}Hf)$ ratios fall within a range of 0.000995–0.004947 and 0.282377~0.282506 (Table S4), respectively. Their $\varepsilon_{Hf}(t)$ values range from −11.3 to −9.5 (mean = −10.5) with a T_{DM1} age of 1167–1268 Ma and T_{DM2} age of 1436–1677 Ma (Figure 9A; Table S4).
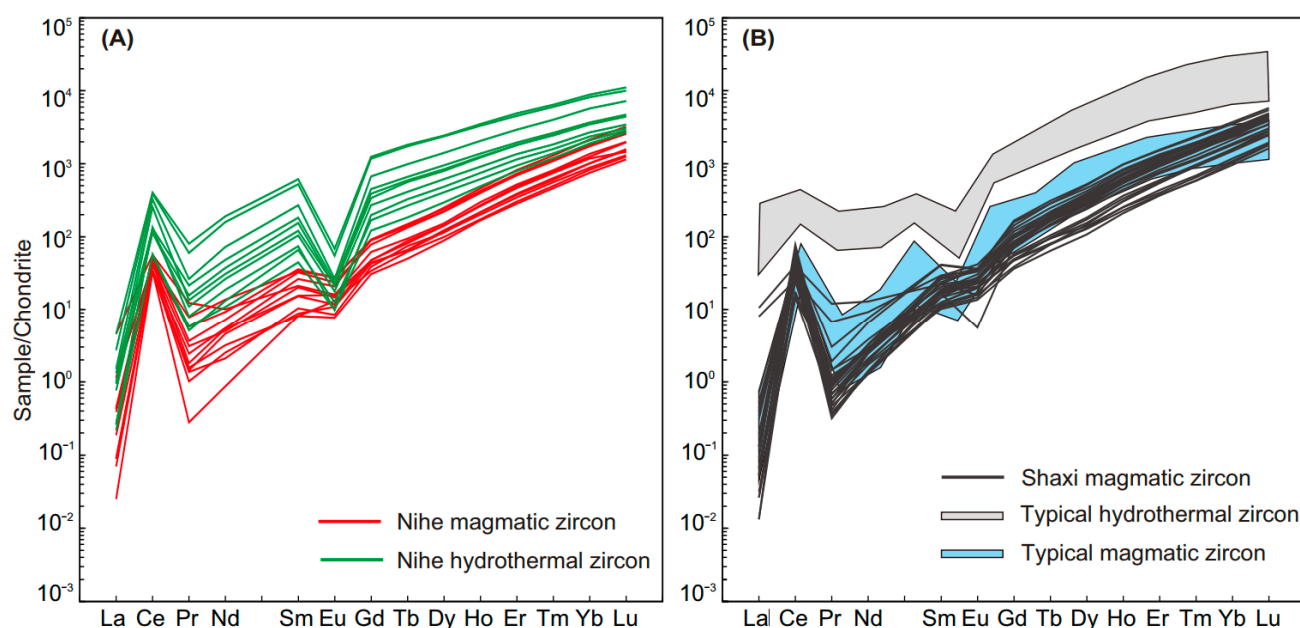

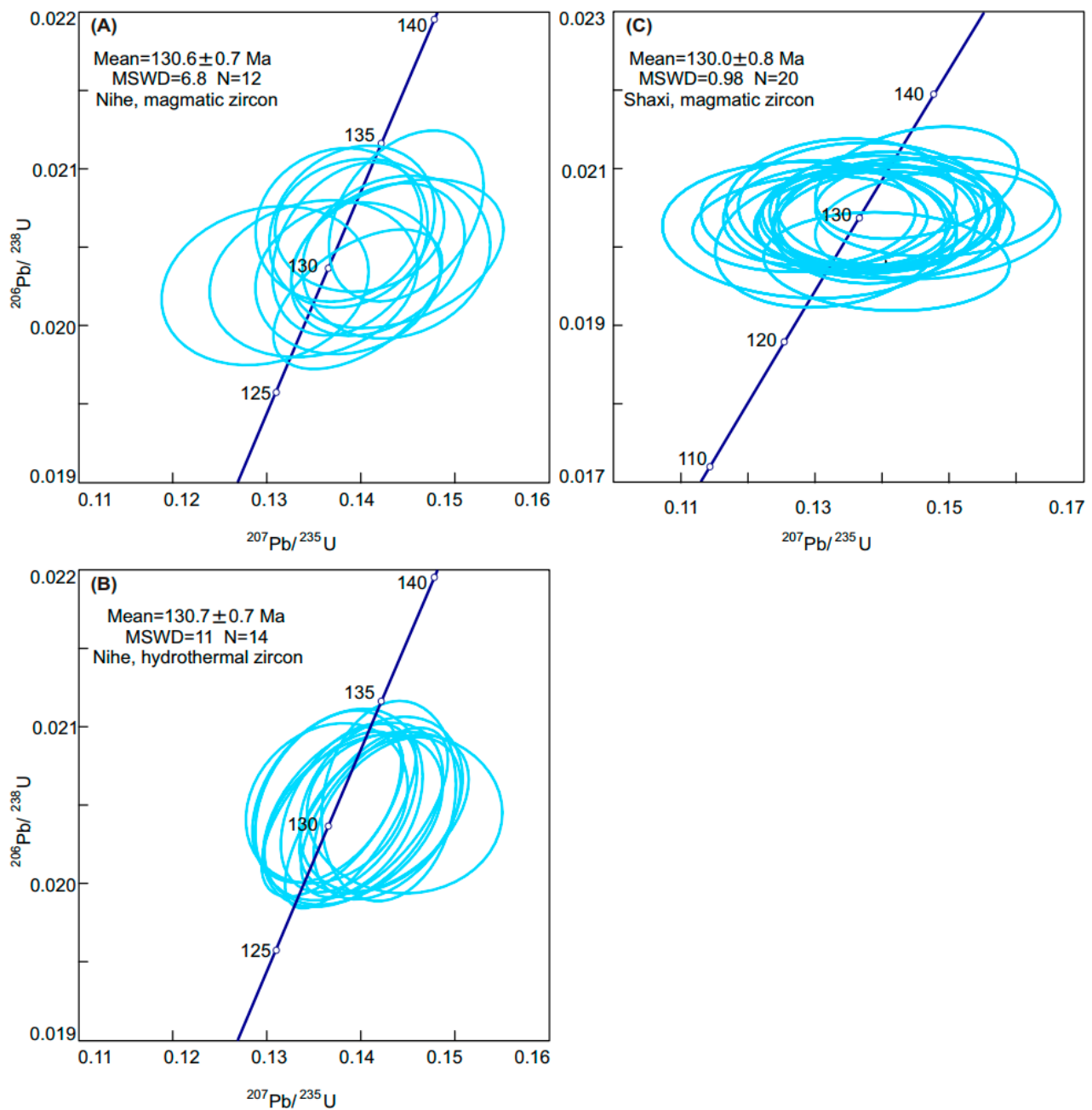**Figure 6.** Chondrite-normalized REE patterns of zircons from the porphyry of Nihe (**A**) and Shaxi (**B**).

Figure 7. Concordia diagrams of LA-ICPMS magmatic zircon U–Pb for Nihe (**A**) and Shaxi (**C**), and hydrothermal zircon U–Pb for Nihe (**B**).
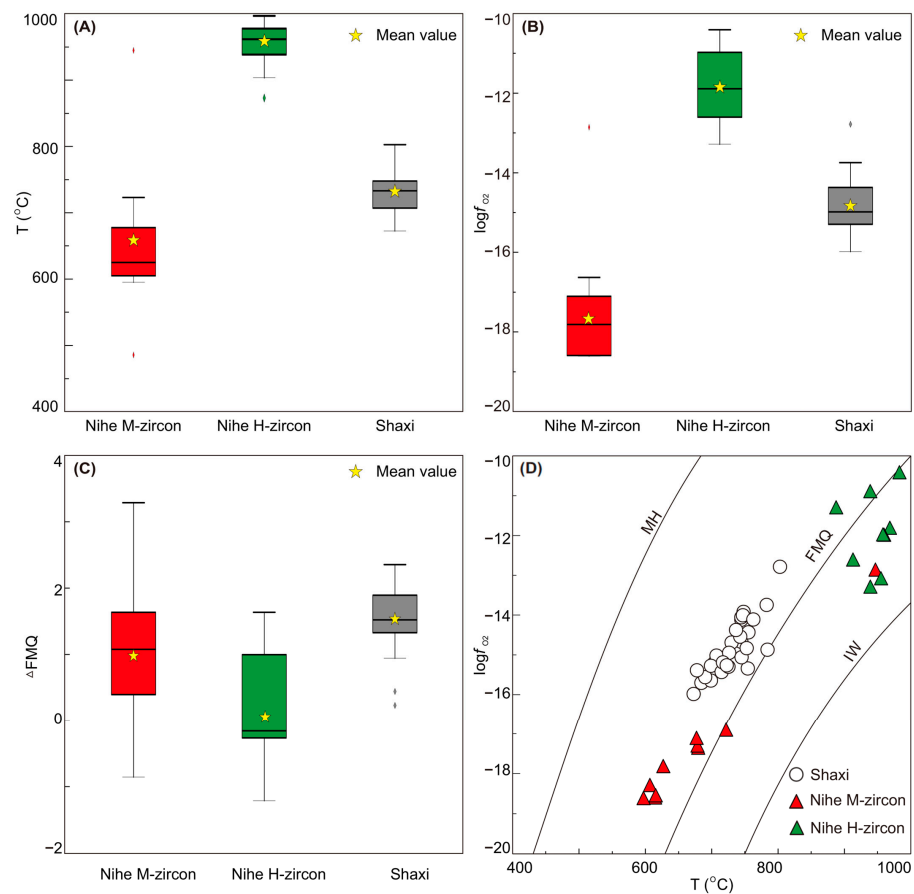
Figure 8. Box plots for zircon crystallization temperature (**A**), log f_{O2} (**B**), and ΔFMQ (**C**). Diagram of zircon T (°C)-log f_{O2} (**D**). The zircon T(°C) and log f_{O2} were calculated using the method of Ferry and Watson [53] and Loucks et al. [54]. Abbreviations: M-zircon = magmatic zircon, H-zircon = hydrothermal zircon.
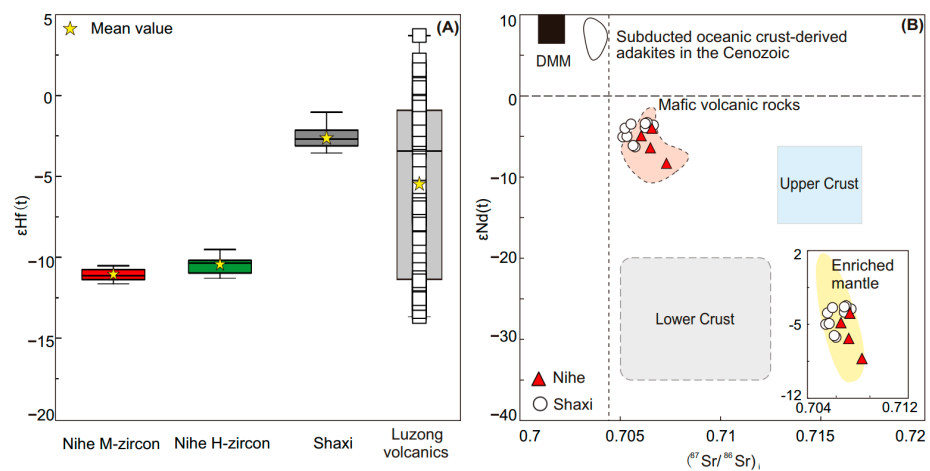
Figure 9. Box plot for zircon εHf(t) of the porphyry in Nihe and Shaxi (**A**). For comparison, the basaltic andesites of the Zhuanqiao Formation at the Luzong Cretaceous volcanic basin [55], Lower Yangtze Valley, are also shown. Initial $^{87}Sr/^{86}Sr$ vs. εNd(t) plot of the porphyries in Nihe and Shaxi (**B**). Data sources for the Cenozoic adakites attributed to the melting of the subducting oceanic crust are from Wang et al. [56], and those for the enriched mantle are from Xie et al. [57]. Abbreviations: M-zircon = magmatic zircon, H-zircon = hydrothermal zircon.

5.2. Shaxi Porphyry Cu–Au Deposit

The biotite crystals of Shaxi are euhedral of 1–2 mm in length, and they are closely associated with chalcopyrite and magnetite (Figure 5D–F). The SiO_2, TiO_2, Al_2O_3, FeO, MnO, MgO, Na_2O, and K_2O of 25 biotite crystals are 36.48–37.84, 4.02–5.99, 13.08–14.54, 14.23–15.45, 0.07–0.31, 14.42–15.98, 0.21–0.6, and 8.69–9.30 wt.%, respectively, with Fe/(Fe + Mg) ratios of 0.34–0.38 (Table S1), indicating that they are magmatic biotites and were not affected by the alteration [58]. The biotites from Shaxi exhibit a temperature and pressure of 638–734 °C and 51.9–129.4 MPa (Table S1), respectively, based on the biotite Al geobarometer [29] and Ti geothermometry [30].

The CL images of zircons from the Shaxi deposit show prominent oscillatory zones (Figure 5G). These zircons have Th and U contents of 106–1109 ppm and 519–1585 ppm, respectively, with Th/U values of 0.2–0.7 (Table S2), indicating that they are typical magmatic zircons [51], which is also supported by the REE characteristics (Figure 6; Table S1). Twenty zircon grains give a concordia age of 130.0 ± 0.8 Ma (MSWD = 0.98; Figure 7C; Table S2). The zircon trace element shows they have LREE-depleted and HREE-enriched characteristics (Figure 6B; Table S1). The average crystallization temperature, f_{O2}, and ΔFMQ of zircons from Shaxi are calculated at 731 °C, −14.82, and 1.54 (Figure 8A–D; Table S3), respectively, based on a zircon Ti thermometer [53] and the f_{O2} equation [54]. In addition, three zircon grains yield the $^{206}Pb/^{238}U$ ages of 790.5 ± 6.4 Ma, 808.1 ± 7.5 Ma, and 809.1 ± 10.0 Ma, respectively (Table S2), indicating that they are inherited zircons.

The $n(^{176}Lu)/n(^{177}Hf)$ and $n(^{176}Hf)/n(^{177}Hf)$ ratios of magmatic zircon from Shaxi fall within a range of 0.001353–0.002505 and 0.282594–0.282668 (Table S4), respectively. Their $\varepsilon_{Hf}(t)$ values range from −3.6 to −1.0 (mean = −2.6) with a T_{DM1} age of 861–942 Ma and T_{DM2} age of 1109–1249 Ma (Figure 9A; Table S4).

6. Discussion

6.1. Temporal–Spatial Relationship between Nihe Fe Deposit and Shaxi Cu–Au Deposit

The Nihe magmatic zircons provide a U–Pb age of 130.6 ± 0.7 Ma (MSWD = 6.8; Figure 7A; Table S2), indistinguishable from previous zircon U–Pb ages, i.e., 132.4 ± 1.5 Ma and 132.8 ± 2.6 Ma [59,60]. The hydrothermal zircon U–Pb age of 130.7 ± 0.7 Ma (MSWD = 11; Figure 7B; Table S2) is consistent with the mineralization age determined by the phlogopite ^{40}Ar-^{39}Ar (130.9 ± 2.6 Ma; [59]). As such, the U–Pb ages are interpreted to represent the emplacement and mineralization ages of the Nihe diorite porphyry. Zircon from the Shaxi porphyry Cu–Au deposit provides a U–Pb age of 130.0 ± 0.8 Ma (MSWD = 0.98; Figure 7C; Table S2). Within uncertainty, it is indistinguishable from previous zircon U–Pb ages, i.e., 129.4 ± 1.4 Ma and 129.5 ± 1.0 Ma [61,62], and the mineralization age determined by the molybdenite Re–Os (130.0 ± 1.0 Ma; [62]). Therefore, the U–Pb age could represent the emplacement and mineralization ages of the Shaxi quartz diorite porphyry. The excellent agreement between the porphyries' emplacement and mineralization ages of the Nihe IOA deposit and the Shaxi porphyry Cu–Au deposit shows that these deposits formed at the same time.

The wall rock of the Nihe IOA deposit (Zhuanqiao Formation; Early Cretaceous) rests above the Shaxi porphyry Cu–Au deposit (Gaojiabian Formation; Early Silurian) according to the law of faunal succession. The crystallization pressures of Nihe clinopyroxene and Shaxi biotite are 39.3–88.9 MPa and 51.9–129.4 MPa, respectively (Table S1). Using the correlation of mineral crystallization pressure and intrusion emplacement depth (100 MPa = 3.3 km), we estimate the mineralization depths of Nihe and Shaxi as 1.0–2.9 km and 1.6–3.9 km, respectively (Table S1). As such, the Nihe IOA deposit has a shallower mineralization depth than that of the Shaxi Cu–Au deposit, which is also supported by the results estimated by available fluid inclusions data. For Nihe, the homogenization temperature and salinity of fluid inclusions in anhydrite at the main mineralization stage are 380–460 °C and 11.3–17.3% NaCl eq., respectively [13], and thus the pressure and corresponding ore-forming depth under lithostatic conditions (~2.5 g/cm^3) can be restricted at 16–40 MPa and 0.8–1.6 km, respectively. For Shaxi, quartz in the potassic stage and

anhydrite in the quartz–sulfide stage were trapped at depths of 0.8–3.2 km and 1.5–2.5 km, respectively [18]. A larger size and a higher proportion of phenocrysts of Shaxi (plagioclase, K–feldspar, amphibole, quartz, and biotite phenocrysts of 1–4 mm in size, accounting for about 45–65% (Figure 5A,B,D,E; [62]) than those of Nihe (phenocrysts of 30–40%, mainly plagioclase and pyroxene with 1–3 mm in size; Figure 4A,B,D,E; [42]) also suggest that the mineralization depth of the Nihe IOA deposit is shallower than that of the Shaxi porphyry Cu–Au deposit. Additionally, this observation was further bolstered by the unique bamboo leaf, vesicular, and other volcanic structures in some IOA deposits [14,63–65].

Based on stratigraphy, petrography, zircon U–Pb dating, biotite–clinopyroxene mineralogical chemistry, and available fluid inclusions research, we suggest that both the Nihe IOA and the Shaxi porphyry Cu–Au deposits formed at 130 Ma, while the former has a shallower mineralization depth. The temporal and spatial coincidence may, by inference, demonstrate a possible genetic link between the Nihe IOA and the Shaxi porphyry Cu–Au deposits.

6.2. Magma Source and Property

The porphyries of Nihe and Shaxi have zircon $\varepsilon_{Hf}(t)$ values ranging from −11.6 to −10.5 and −3.6 to −1.0, respectively (Figure 9A and Table S4), which are significantly higher than those of lower crust basement rocks in the Yangtze craton (εHf (120–150Ma) = −70.8~−61.8; [57,66]). Therefore, the ore-forming magma of Nihe and Shaxi cannot be originated from the partial melting of the lower crust basement. Specifically, the magmatic zircons and hydrothermal zircons from Nihe have similar $\varepsilon_{Hf}(t)$ values ranging from −11.6 to −10.5 and from −11.3 to −9.5, respectively (Figure 9A; Table S4). The zircon $\varepsilon_{Hf}(t)$ values of mineralization-related porphyry at Nihe (−11.6~−10.5) and Shaxi (−3.6~−1.0) overlap with the range of the Zhuanqiao Formation volcanic rocks in the Luzong area (−13.6~+3.7; Figure 9A; [55]) that derived from an enriched lithosphere mantle. In addition, the $\varepsilon_{Nd}(t)$ and $(^{87}Sr/^{86}Sr)_i$ values of Nihe Fe-related diorite porphyry range from −8.3 to −4.0 and from 0.7060 to 0.7073 (Figure 9B; [67]), respectively, resembling those of the Shaxi Cu–Au mineralization-related quartz diorite porphyry (−6.7 to −3.3 and 0.7051 to 0.7066; Figure 9B; [68–70]). The similar Sr–Nd isotopic characteristics of Nihe and Shaxi are significantly different from those of the lower crust of the Yangtze craton and the Cenozoic adakites derived from the subducted oceanic crust [56], while overlapping the range of contemporary basic volcanic rocks and enriched mantle (Figure 9B; [57]). Additionally, the magmatic zircons of Nihe showed similar REE characteristics with zircons from Shaxi, which also indicates that they may evolve from a similar magma source (Figure 6A,B). As such, the relatively negative $\varepsilon_{Hf}(t)$ values and enriched Sr–Nd isotopic characteristics suggest an enriched lithospheric mantle source for the porphyries from both Nihe and Shaxi.

However, it should be noted that the Cu–Au mineralization-related porphyry at Shaxi has higher zircon $\varepsilon_{Hf}(t)$ values than that of the Fe mineralization-related porphyry at Nihe (Figure 9A). This difference may be reflected by the contamination of the Jiangnan-type basement ($\varepsilon Hf(t)$ = +4.4~+7.9; [68]) in the Shaxi Cu–Au mineralization-related magma. This possibility has been supported by three ancient zircon grains at Shaxi ($^{206}Pb/^{238}U$ age of 791–809 Ma; Table S5), which were likely inherited from the Jiangnan-type basement, while no ancient zircon was found in the Nihe IOA deposit. Therefore, we believe that the porphyries of both Nihe and Shaxi originated from the enriched lithospheric mantle, although there is some contribution of lower crustal materials from the Jiangnan-type basement to the Shaxi Cu–Au deposit.

The Nihe magmatic zircon has a lower average crystallization temperature and f_{O2} (657 °C and −17.66; Figure 8A,B; Table S3) but a higher average ΔFMQ (0.99) than that of hydrothermal zircon (951 °C, −11.84, and 0.06; Figure 8A,C,D; Table S3). The f_{O2} is a function of temperature and thus will vary with temperature, which may cause misunderstanding when comparing the magma oxidation state of different intrusions. As such, it is better to use ΔFMQ to compare the magma oxidation state rather than f_{O2}. The average ΔFMQ of the Shaxi quartz diorite porphyry (1.54; Figure 8C,D; Table S3) is slightly higher than that

of the Nihe diorite porphyry (0.99; Figure 8C,D; Table S3), indicating that the ore-related magma of Shaxi is more oxidized than that of Nihe, which is further supported by the zircon Eu/Eu* values (Figure 10A; [71]). Notably, the lower ΔFMQ of the Nihe diorite porphyry does not contradict the idea that the IOA deposits are precipitated from heavily oxidized hydrothermal fluids [42,72]. Previous research reported that the magma oxidation state of IOA is changeable during the mineralization process, i.e., the primary magma of an IOA deposit with low oxygen fugacity will increase as a result of contamination of the P-rich or gypsum strata [42,72,73]. Furthermore, the variation of negative Eu anomalies in titanite also suggests increasing oxygen fugacity of metalliferous fluids from deep to shallow in the IOA deposit [15,74].
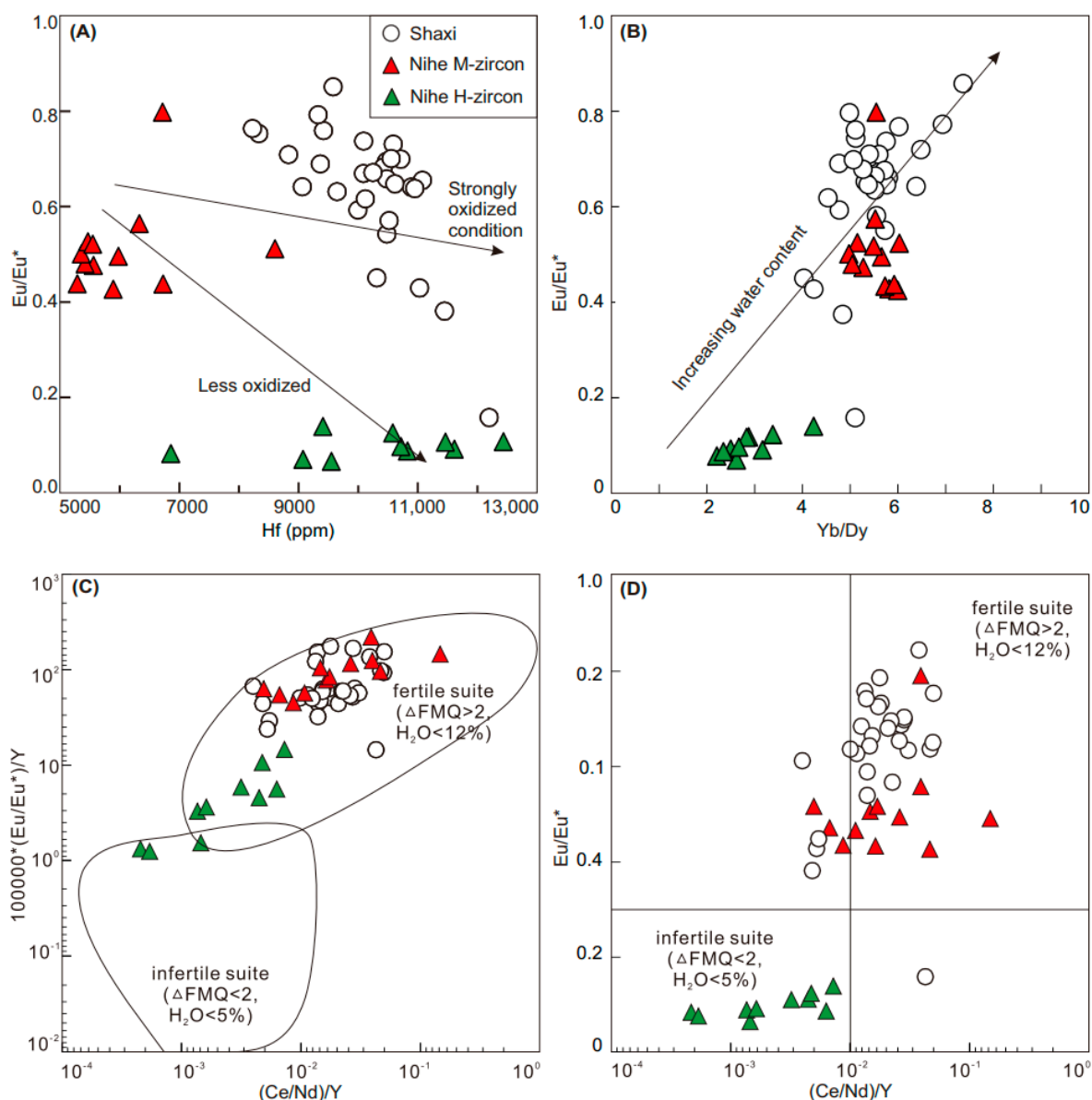

Figure 10. Diagram of zircon trace elements on Hf vs. Eu/Eu* [71] (**A**) and Yb/Dy vs. Eu/Eu* [24] (**B**). Diagram of zircon Eu/Eu* vs. (Ce/Nd)/Y (**C**) and 10,000 × (Eu/Eu*)/Y vs. (Ce/Nd)/Y (**D**). The zircon trace element ranges to define high oxygen fugacity–high water content fertile magma (ΔFMQ > 2 and H$_2$O < 12%) and low oxygen fugacity–low water content (ΔFMQ < 2 and H$_2$O < 5%) infertile suite refer to [20]. Abbreviations: M-zircon = magmatic zircon, H-zircon = hydrothermal zircon.

Hafnium has almost the same radius and charge as Zr, so it can replace Zr in zircon, and the Hf/Zr ratio of the zircon is generally controlled by the degree of magmatic fractionation [75,76]. As shown in Figure 10A, the zircon Hf content of Shaxi is higher than that of Nihe, indicating that the degree of magma fractionation of the Shaxi porphyry deposit is stronger than that of the Nihe. The fractional crystallization of amphibole and plagioclase will increase the Yb/Dy ratio and negative Eu anomalies in the residual melt; thus, the zircon Yb/Dy and Eu/Eu* ratios can be controlled by magmatic hydrous states [20,24,77]. As shown in Figure 10B, the trend of zircon Yb/Dy and Eu/Eu* ratios likely suggest that the porphyry of Shaxi has a slightly higher magma water content (Table S3; [20,24]). As the IOA deposits are usually near the deep fault, the ore-related magma may migrate through the fault quickly, resulting in a small degree of magma fractionation and low magma water content.

6.3. Implications for the Genetic Link between IOA and Porphyry Cu–Au Deposits and Their Mineral Exploration

Previous studies accepted that the ore-forming magmas of the IOA deposits at MLYRMB were generated from an enriched lithospheric mantle [31,41,73,78] as well as the Shaxi Cu–Au deposit [19,69,70]. Our zircon U–Pb dating and Hf isotope data further confirm this opinion and show that the Nihe and Shaxi deposits are derived from a common magma source at 130 Ma, indicating that both two deposits are temporal–spatially and genetically related. Considering the higher zircon εHf(t) values and the existence of inherited zircon (791–809 Ma) at Shaxi, some contribution of the Jiangnan-type basement was involved at the Shaxi Cu–Au deposit, which has been reported by previous research [19,69,70]. Zircon trace element data measured by this study indicated that the Nihe IOA deposit has a weaker fractionation degree and lower ΔFMQ and magma water content than that of the Shaxi Cu–Au deposit. These differences may be controlled by the deep fault near the IOA deposits, which also caused the shallower emplacement depth of the IOA deposit as determined by the stratigraphy, petrography, mineral barometers, and available fluid inclusion research [13,18,42,62].

Zircon (Eu/Eu*)/Y and (Ce/Nd)/Y ratios are effective fertility indicators for magmas [20,22,24], and the (Eu/Eu*)/Y and (Ce/Nd)/Y ratios of magmatic zircons of ore-related porphyries from Nihe and Shaxi overlap with the range of fertile magma (Figure 10C,D). Additionally, a magmatic-hydrothermal Cu–Au deposit has been discovered around the Meishan IOA deposits [4,79], which indicates that the IOA-forming magma also has the potential to coexist with magmatic-hydrothermal Cu–Au deposits, similar to various mineralization types developed in porphyry Cu systems [2].

Interestingly, the porphyry deposits in the MLYRMB have the same characteristics of linear cluster and periodic mineralization as typical porphyry deposits [19,35,36]. Furthermore, relatively high contents of the platinum-group element (PGE) have developed in the porphyry Cu–Au systems, for instance, Santo Tomas II in Philippines [80] and Dexing in China [81], especially in the magnetite-bearing assemblages of potassic alteration zones [82]. The Shaxi Cu–Au deposit has some geological features similar to the PGE-rich porphyry systems, e.g., ore-related intrusion, Au-enrichment, high sulfide content, and extensive potassic alteration with magnetite-rich assemblages (Figures 2 and 5A–F; [18,45,62,80,82]), indicating a potential for PGE prospecting in the Shaxi porphyry Cu–Au deposit. Additionally, the Shaxi Cu–Au deposit is the only porphyry Cu–Au deposit formed during middle-stage porphyry mineralization (133–125 Ma) in the MLYRMB so far [17–19,45]. According to the spatial relationship and the temporal and genetic link between the porphyry and IOA, there is great potential for prospecting porphyry Cu–Au-PGE deposits (between 133–125 Ma) in the MLYRMB [11,19,37,38] and other areas that contain IOA deposits in similar tectonic settings; specifically, in the deep part of the IOA district in the Luzong Cretaceous volcanic basin, Lower Yangtze Valley.

7. Conclusions

Based on the Nihe IOA and the Shaxi porphyry Cu–Au deposits in the Lower Yangtze Valley, we established a temporal–spatial and possible genetic link between IOA and porphyry Cu–Au deposits using EPMA of clinopyroxene and biotite, and zircon U–Pb dating, Hf isotopes, and trace elements. The excellent agreement between the porphyry emplacement and mineralization ages of Nihe (130.6 ± 0.7 Ma and 130.7 ± 0.7 Ma) and Shaxi (130.0 ± 0.8 Ma and 130.0 ± 1.0 Ma) demonstrates a simultaneity. All the stratigraphy, petrography, biotite–clinopyroxene mineralogical chemistry, and available fluid inclusion results indicate that the emplacement depth of the Nihe IOA deposit is shallower than the Shaixi Cu–Au deposit. The zircon εHf(t) values indicate that both Nihe ($-11.6\sim-9.5$) and Shaxi ($-3.6\sim-1.0$) derived from the enriched lithospheric mantle, with some contributions of crustal materials from the Jiangnan-type basement to the Shaxi porphyry Cu–Au deposit. The differences in crustal contamination, degree of magma fractionation, magma oxidation, and water content are the possible factors leading to the differences between Nihe and Shaxi. Our study establishes a temporal–spatial and possible genetic link between IOA and porphyry Cu–Au deposits and highlights that there is a huge potential for prospecting porphyry Cu–Au-PGE deposits in the MLYRMB, especially in the deep part of the IOA district in the Luzong Cretaceous volcanic basin, Lower Yangtze Valley.

Supplementary Materials: The following supporting information can be downloaded at: https://www.mdpi.com/article/10.3390/min13030451/s1. Table S1: EPMA data of clinopyroxene from the IOA deposit and biotite from the Shaxi Cu–Au deposit. Table S2: The zircon LA-ICP-MS U-Pb dating from the Nihe IOA deposit and the Shaxi Cu–Au deposit. Table S3: In situ trace element data of zircon from the Nihe IOA deposit and the Shaxi Cu–Au deposit. Table S4: In situ Hf isotopic data of zircon from the Nihe IOA deposit and the Shaxi Cu-Au deposit.

Author Contributions: Y.L. and K.-Z.Q. conceived this contribution and conducted all the analytical work, assisted by G.-X.S., Y.F. and F.-Y.W. The manuscript was written by Y.L. and revised by L.W. and G.-X.S. with contribution from K.-Z.Q. All authors have read and agreed to the published version of the manuscript.

Data Availability Statement: Data supporting reported results can be found in Supplementary Materials.

Conflicts of Interest: The authors declare no conflict of interest.

References

1. Hedenquist, J.W.; Lowenstern, J.B. The role of magmas in the formation of hydrothermal ore-deposits. *Nature* **1994**, *370*, 519–527. [CrossRef]
2. Sillitoe, R.H. Porphyry copper systems. *Econ. Geol.* **2010**, *105*, 3–41. [CrossRef]
3. Einaudi, M.T. Description of skarns associated with porphyry copper plutons. In *Advances in Geology of the Porphyry Copper Deposits, Southwestern North America*; University of Arizona Press: Tucson, AZ, USA, 1982.
4. Yu, J.J.; Che, L.R.; Wang, T.Z. Alteration, oxygen isotope, and fluid inclusion study of the Meishan iron oxide–apatite deposit, SE China. *Miner. Depos.* **2015**, *50*, 847–869. [CrossRef]
5. Hu, H.; Li, J.W.; Harlov, D.E.; Lentz, D.R.; McFarlane, C.R.M.; Yang, Y.H. A genetic link between iron oxide-apatite and iron skarn mineralization in the Jinniu volcanic basin, Daye district, eastern China: Evidence from magnetite geochemistry and multi-mineral U-Pb geochronology. *GSA Bull.* **2020**, *132*, 899–917. [CrossRef]
6. Liu, Y.N.; Fan, Y.; Zhou, T.F.; Xiao, X.; White, N.C.; Thompson, J.; Hong, H.L.; Zhang, L.J. Geochemical characteristics of magnetite in Longqiao skarn iron deposit in the Middle-Lower Yangtze Metallogenic Belt, Eastern China. *Miner. Depos.* **2019**, *54*, 1229–1242. [CrossRef]

7.　Mao, J.W.; Wang, Y.T.; Lehmann, B.; Yu, F.; Du, A.D.; Mei, Y.X.; Li, Y.X.; Zang, W.S.; Stein, H.J.; Zhou, T.F. Molybdenite Re–Os and albite ⁴⁰Ar-³⁹Ar dating of Cu–Au–Mo and magnetite porphyry systems in the Yangtze River valley and metallogenic implications. *Ore Geol. Rev.* **2006**, *29*, 307–324. [CrossRef]

8.　Pan, Y.M.; Dong, P. The lower Changjiang (Yangzi/Yangtze River) metallogenic belt, east central China: Intrusion and wall rock hosted Cu-Fe-Au, Mo, Zn, Pb, Ag deposits. *Ore Geol. Rev.* **1999**, *15*, 177–242. [CrossRef]

9.　Zhou, T.F.; Fan, Y.; Wang, S.W.; White, N.C. Metallogenic regularity and metallogenic model of the Middle-Lower Yangtze River Valley Metallogenic Belt. *Acta Petrol. Sin.* **2017**, *33*, 3353–3372. (In Chinese)

10.　Chang, Y.F.; Liu, X.P.; Wu, C.Y. *Cu-Fe Metallogenic Belt in the Middle and Lower Reaches of Yangtze River*; Geological Press: Beijing, China, 1991; pp. 71–76.

11.　Wang, Z.T.; Qin, K.Z. Types, Metallogenic Environments and Characteristics of Temporal and Spatial Distribution of Copper Deposits in China. *Acta Geol. Sin. Engl. Ed.* **1989**, *2*, 79–92.

12.　Qin, K.Z.; Zhai, M.G.; Li, G.M.; Zhao, J.X.; Zeng, Q.D.; Gao, J.; Xiao, W.J.; Li, J.L.; Sun, S. Links of Collage orogenesis of microcontinents and crust evolution to characteristic metallogeneses in China. *Acta Petrol. Sin.* **2017**, *33*, 305–325. (In Chinese)

13.　Fan, Y.; Zhou, T.F.; Hao, L.; Yuan, F.; Zhang, L.J.; Wang, W.C. Ore-forming fluid characteristic of Nihe iron deposit in Lu-Zong basin, Anhui Province and its significance to ore genesis. *Acta Petrol. Sin.* **2012**, *28*, 3113–3124. (In Chinese)

14.　Li, W.T.; Audétat, A.; Zhang, J. The role of evaporites in the formation of magnetite–apatite deposits along the Middle and Lower Yangtze River, China: Evidence from LA-ICP-MS analysis of fluid inclusions. *Ore Geol. Rev.* **2015**, *67*, 264–278. [CrossRef]

15.　Liu, Y.N.; Fan, Y.; Zhou, T.F.; Zhang, L.J.; White, N.C.; Hong, H.L.; Zhang, W. LA-ICP-MS titanite U-Pb dating and mineral chemistry of the Luohe magnetite-apatite (MA)-type deposit in the Lu-Zong volcanic basin, Eastern China. *Ore Geol. Rev.* **2018**, *92*, 284–296. [CrossRef]

16.　Ren, Q.J.; Liu, X.S.; Xu, Z.W. *Mesozoic Volcanic Tectonic Depression and Mineralization in Luzong, Anhui Province*; Geological Press: Beijing, China, 1991.

17.　Nie, L.Q.; Zhou, T.F.; Fan, Y.; Zhang, L.J.; Cooke, D.; White, N. Geology, geochemistry and genesis of the Makou magnetite-apatite deposit in the Luzong volcanic basin, Middle-Lower Yangtze River Valley Metallogenic Belt, Eastern China. *Ore Geol. Rev.* **2017**, *91*, 264–277. [CrossRef]

18.　Wang, S.W.; Zhou, T.F.; Hollings, P.; Yuan, F.; Fan, Y.; White, N.C.; Zhang, L.J. Ore genesis and hydrothermal evolution of the Shaxi porphyry Cu–Au deposit, Anhui province, Eastern China: Evidence from isotopes (S–Sr–H–O), pyrite, and fluid inclusions. *Miner. Depos.* **2021**, *56*, 767–788. [CrossRef]

19.　Zhou, T.F.; Wang, S.W.; Fan, Y.; Yuan, F.; Zhang, D.Y.; White, N.C. A review of the intracontinental porphyry deposits in the Middle-Lower Yangtze River Valley metallogenic belt, Eastern China. *Ore Geol. Rev.* **2015**, *65*, 433–456. [CrossRef]

20.　Lu, Y.J.; Loucks, R.R.; Fiorentini, M.; Mccuaig, T.C.; Evans, N.J.; Yang, Z.M.; Hou, Z.Q.; Kirkland, C.L.; Parra-Avila, L.A.; Alankobussen. Zircon as pathfinder to pophyry Cu ± Mo ± Au mineral deposits. *Soc. Econ. Geol. Spec. Publ.* **2016**, *19*, 329–347.

21.　Belousova, E.A.; Griffin, W.L.; O'Reilly, S.Y.; Fisher, N.I. Igneous zircon: Trace element composition as an indicator of source rock type. *Contrib. Mineral. Petrol.* **2002**, *143*, 602–622. [CrossRef]

22.　Zhao, J.X.; Su, B.X.; Uysal, I.; Aydin, F.; Xiao, Y.; Sen, C.; Hui, K.X.; Qin, K.Z. Evolution of magma oxidation states and volatile components in the Cenozoic porphyry ore systems in the western Turkey, Tethyan domain: Constrains from the compositions of zircon and apatite. *Acta Petrol. Sin.* **2021**, *37*, 2339–2363. (In Chinese)

23.　Zou, X.Y.; Jiang, J.L.; Qin, K.Z.; Zhang, Y.G.; Yang, W.; Li, X.H. Progress in the principle and application of zircon trace element. *Acta Petrol. Sin.* **2021**, *37*, 985–999. (In Chinese)

24.　Wen, G.; Zhou, R.J.; Li, J.W.; Chang, J.; Hu, H.; Yan, D.R.; Wei, K.T.; Jin, S.G. Skarn metallogeny through zircon record: An example from the Daye Cu-Au-Fe-Mo district, eastern China. *Lithos* **2020**, *378–379*, 105807. [CrossRef]

25.　Valley, P.M.; Fisher, C.M.; Hanchar, J.M.; Lam, R.; Tubrett, M. Hafnium isotopes in zircon: A tracer of fluid-rock interaction during magnetite-apatite ("Kiruna-type") mineralization. *Chem. Geol.* **2010**, *275*, 208–220. [CrossRef]

26.　Song, G.X.; Qin, K.Z.; Li, G.M.; Evans, N.J.; Li, X.H. Mesozoic magmatism and metallogeny in the Chizhou area, Middle-Lower Yangtze Valley, SE China: Constrained by petrochemistry, geochemistry and geochronology. *J. Asian Earth Sci.* **2014**, *91*, 137–153. [CrossRef]

27.　Putirka, K.D. Thermometers and Barometers for Volcanic Systems. *Rev. Mineral. Geochem.* **2008**, *69*, 61–120. [CrossRef]

28.　Wang, X.D.; Hou, T.; Wang, M.; Zhang, C.; Zhang, Z.C.; Pan, R.H.; Marxer, F.; Zhang, H.L. A new clinopyroxene thermobarometer for mafic to intermediate magmatic systems. *Eur. J. Mineral.* **2021**, *33*, 621–637. [CrossRef]

29.　Uchida, E.; Endo, S.; Makino, M. Relationship between solidification depth of granitic rocks and formation of hydrothermal ore deposits. *Resour. Geol.* **2007**, *57*, 47–56. [CrossRef]

30.　Henry, D.J.; Guidotti, C.V.; Thomson, J.A. The Ti-saturation surface for low-to-medium pressure metapelitic biotites: Implications for geothermometry and Ti-substitution mechanisms. *Am. Mineral.* **2005**, *90*, 316–328. [CrossRef]

31.　Li, Y.; Li, Y.; Wang, C.M.; Li, X.H. Temporal-spatial coincidence may not always discern causality: Insights from two skarn deposits in Anqing and Zhibula, China. *Ore Geol. Rev.* **2022**, *146*, 104951. [CrossRef]

32.　Mao, J.W.; Xie, G.Q.; Duan, C.; Pirajno, F.; Ishiyama, D.; Chen, Y.C. A tectono-genetic model for porphyry-skarn-stratabound Cu-Au-Mo-Fe and magnetite-apatite deposits along the Middle-Lower Yangtze River Valley, Eastern China. *Ore Geol. Rev.* **2011**, *43*, 294–314. [CrossRef]

33.   Li, G.M.; Qin, K.Z.; Song, G.X.; Bagas, L. The oldest Mo porphyry mineralization in the Yangtze Valley Metallogenic Belt of eastern China: Constraints on its origin from geochemistry, geochronology and fluid inclusion studies at Matou. *Ore Geol. Rev.* **2017**, *91*, 491–508. [CrossRef]

34.   Song, G.; Qin, K.; Li, G.; Liu, T.; Li, J.; Li, X.; Chang, Z. Geochronologic and isotope geochemical constraints on magmatism and associated W–Mo mineralization of the Jitoushan W–Mo deposit, middle–lower Yangtze Valley. *Int. Geol. Rev.* **2012**, *54*, 1532–1547. [CrossRef]

35.   Sillitoe, R.H.; Perelló, J. Andean Copper Province: Tectonomagmatic Settings, Deposit Types, Metallogeny, Exploration, and Discovery. In *Econ. Geol. 100th Anniversary Volume*; Society of Economic Geologists, Inc.: Littleton, CO, USA, 2005.

36.   Hou, Z.Q.; Duan, L.F.; Lu, Y.J.; Zheng, Y.C.; Zhu, D.C.; Yang, Z.M.; Yang, Z.S.; Wang, B.D.; Pei, Y.R.; Zhao, Z.D.; et al. Lithospheric architecture of the Lhasa Terrane and its control on ore deposits in the Himalayan-Tibetan Orogen. *Econ. Geol.* **2015**, *110*, 1541–1575. [CrossRef]

37.   Li, W.D.; Wang, W.B.; Fan, H.Y.; Dong, P.; Zhou, T.F.; Xie, H.G. The formation conditions of copper (gold) deposits in the Middle-Lower Yangtze River metallogenic belt and the possibility of the existence of ultra-large deposits. *Volcan. Geol. Miner.* **1997**, *20*, 11–31. (In Chinese)

38.   Tang, Y.C.; Wu, C.Y.; Chu, G.Z. *Copper-Gold Polymetallic Deposits Along the River in Anhui*; Geological Press: Beijing, China, 1998.

39.   Tang, J.F.; Lu, S.M.; Li, J.S.; Wei, D.Z. The basement structural deformation, evolution and its control action on deposit distribution in Luzong volcanic basin and its adjacent area in Anhui Province, China. *Acta Petrol. Sin.* **2010**, *26*, 2587–2597. (In Chinese)

40.   Zhou, T.F.; Fan, Y.; Yuan, F.; Lu, S.M.; Shang, S.G.; Cooke, D.; Meffre, S.; Zhao, G.C. Geochronology of the volcanic rocks in the Lu-Zong basin and its significance. *Sci. China Ser. D Earth Sci.* **2008**, *51*, 1470–1482. [CrossRef]

41.   Zhou, T.F.; Fan, Y.; Yuan, F.; Zhang, L.J.; Qian, B.; Ma, L.; Yang, X.F. Geology and geochronology of magnetite-apatite deposits in the Ning-Wu volcanic basin, eastern China. *J. Asian Earth Sci.* **2013**, *66*, 90–107. [CrossRef]

42.   Wu, M.G.; Zhang, Y.Y.; Zhao, W.G.; Fan, Y.; Wang, L.Y.; Wei, G.H.; Wang, K.Y.; Che, Y.D. Geological characteristics and genesis of the Nihe Fe-S deposit, Lujiang district, Anhui Province. *Acta Geol. Sin.* **2011**, *85*, 789–801. (In Chinese)

43.   Liu, Y.N.; Fan, Y.; Zhang, L.J. Precipitation mechanism, REE characteristics of anhydrite in Nihe deposit and its relation to mineralization. *Acta Petrol. Sin.* **2017**, *33*, 3531–3544. (In Chinese)

44.   Zhou, T.F.; Fan, Y.; Yuan, F.; Wu, M.A.; Zhao, W.G.; Qian, B.; Ma, L.; Wang, W.C.; Liu, Y.N.; Noel, W. The metallogenic model of Nihe iron deposit in Lu-Zong basin and genetic relationship between gypsum-salt layer and deposit. *Acta Geol. Sin.* **2014**, *88*, 562–573. (In Chinese)

45.   Yuan, F.; Zhou, T.F.; Wang, S.W.; Fan, Y.; Tang, C.; Zhang, Q.M.; Yu, C.H.; Shi, C. Characteristics of alteration and mineralization of the Shaxi porphyry copper deposit, Luzong area, Anhui Province. *Acta Petrol. Sin.* **2012**, *28*, 3099–3112. (In Chinese)

46.   Liu, Y.S.; Gao, S.; Hu, Z.C.; Gao, C.G.; Zong, K.Q.; Wang, D.B. Continental and Oceanic Crust Recycling-induced Melt-Peridotite Interactions in the Trans-North China Orogen: U-Pb Dating, Hf Isotopes and Trace Elements in Zircons from Mantle Xenoliths. *J. Petrol.* **2010**, *51*, 537–571. [CrossRef]

47.   Vermeesch, P. IsoplotR: A free and open toolbox for geochronology. *Geosci. Front.* **2018**, *9*, 1479–1493. [CrossRef]

48.   Hu, Z.C.; Liu, Y.S.; Gao, S.; Liu, W.G.; Zhang, W.; Tong, X.R.; Lin, L.; Zong, K.Q.; Li, M.; Chen, H.H.; et al. Improved in situ Hf isotope ratio analysis of zircon using newly designed X skimmer cone and jet sample cone in combination with the addition of nitrogen by laser ablation multiple collector ICP-MS. *J. Anal. At. Spectrom.* **2012**, *27*, 1391–1399. [CrossRef]

49.   Fisher, C.M.; Vervoort, J.D.; Hanchar, J.M. Guidelines for reporting zircon Hf isotopic data by LA-MC-ICPMS and potential pitfalls in the interpretation of these data. *Chem. Geol.* **2014**, *363*, 125–133. [CrossRef]

50.   BlichertToft, J.; Chauvel, C.; Albarede, F. Separation of Hf and Lu for high-precision isotope analysis of rock samples by magnetic sector multiple collector ICP-MS. *Contrib. Mineral. Petrol.* **1997**, *127*, 248–260. [CrossRef]

51.   Wu, Y.B.; Zheng, Y.F. Genesis of zircon and its constraints on interpretation of U-Pb age. *Chin. Sci. Bull.* **2004**, *49*, 1554–1569. (In Chinese)

52.   Hoskin, P.W.O. Trace-element composition of hydrothermal zircon and the alteration of Hadean zircon from the Jack Hills, Australia. *Geochim. Cosmochim. Acta* **2005**, *69*, 637–648. [CrossRef]

53.   Ferry, J.M.; Watson, E.B. New thermodynamic models and revised calibrations for the Ti-in-zircon and Zr-in-rutile thermometers. *Contrib. Mineral. Petrol.* **2007**, *154*, 429–437. [CrossRef]

54.   Loucks, R.R.; Fiorentini, M.L.; Henriquez, G.J. New Magmatic Oxybarometer Using Trace Elements in Zircon. *J. Petrol.* **2020**, *61*, egaa034. [CrossRef]

55.   Chen, L.; Zhao, Z.F.; Zheng, Y.F. Origin of andesitic rocks: Geochemical constraints from Mesozoic volcanics in the Luzong basin, South China. *Lithos* **2014**, *190*, 220–239. [CrossRef]

56.   Wang, Q.; Xu, J.F.; Jian, P.; Bao, Z.W.; Zhao, Z.H.; Li, C.F.; Xiong, X.L.; Ma, J.L. Petrogenesis of adakitic porphyries in an extensional tectonic setting, dexing, South China: Implications for the genesis of porphyry copper mineralization. *J. Petrol.* **2006**, *47*, 119–144. [CrossRef]

57.   Xie, G.Q.; Mao, J.W.; Zhao, H.J. Zircon U–Pb geochronological and Hf isotopic constraints on petrogenesis of Late Mesozoic intrusions in the southeast Hubei Province, Middle–Lower Yangtze River belt (MLYRB), East China. *Lithos* **2011**, *25*, 693–710. [CrossRef]

58.   Stone, D. Temperature and pressure variations in suites of Archean felsic plutonic rocks, Berens river area, northwest superior province, Ontario, Canada. *Can. Mineral.* **2000**, *38*, 455–470. [CrossRef]

59. Fan, Y.; Liu, Y.N.; Zhou, T.F.; Zhang, L.J.; Yuan, F.; Wang, W.C. Geochronology of the Nihe deposit and in the Lu-Zong basin and its metallogenic significances. *Acta Petrol. Sin.* **2014**, *30*, 1369–1381. (In Chinese)

60. Qin, Y.J.; Zeng, J.N.; Zeng, Y.; Ma, Z.D.; Chen, J.H.; Jin, X. Zircon LA-ICP-MS U-Pb dating of ore-bearing pyroxene-trachyandesite porphyry and its geological significance in Luohe-Nihe iron ore field in Luzong basin, southern Anhui, China. *Geol. Bull. China* **2010**, *29*, 851–862. (In Chinese)

61. Tang, C.; Zhou, T.F.; Yuan, F.; Fan, Y.; Wang, S.W. Geological characteristics and formation era of Shaxi copper deposit in Lujiang district, Anhui Province. *Acta Mineral. Sin.* **2011**, *31*, 91–92. (In Chinese)

62. Wang, S.W.; Zhou, T.F.; Yuan, F.; Fan, Y.; Yu, C.H.; Ge, L.H.; Shi, C.; Chi, Y.Y. Emplacement sequences and geochronology of the Shaxi porphyry copper-gold deposit. *Acta Petrol. Sin.* **2014**, *30*, 979–994. (In Chinese)

63. Ningwu Research Group. *Magnetite Porphyry Deposits in Ningwu Area*; Geological Press: Beijing, China, 1978.

64. Tornos, F.; Velasco, F.; Hanchar, J.M. Iron-rich melts, magmatic magnetite, and superheated hydrothermal systems: The El Laco deposit, Chile. *Geology* **2016**, *44*, 427–430. [CrossRef]

65. Mungall, J.E.; Long, K.; Brenan, J.M.; Smythe, D.; Naslund, H.R. Immiscible shoshonitic and Fe-P-oxide melts preserved in unconsolidated tephra at El Laco volcano, Chile. *Geology* **2018**, *46*, 255–258. [CrossRef]

66. Zhang, S.B.; Zheng, Y.F.; Wu, Y.B.; Zhao, Z.F.; Gao, S.; Wu, F.Y. Zircon isotope evidence for >= 3.5 Ga continental crust in the Yangtze craton of China. *Precambrian Res.* **2006**, *146*, 16–34. [CrossRef]

67. Yang, S.X.; Zhang, J.Y.; Zhang, Z.Z.; Wei, G.H. Geochemical characteristics of ore-bearing diorite porphyrite of the Nihe iron ore deposit in Lujiang, Anhui province. *East China Geol.* **2017**, *38*, 241–249. (In Chinese)

68. Deng, J.H.; Yang, X.Y.; Li, S.; Gu, H.L.; Mastoi, A.S.; Sun, W.D. Partial melting of subducted paleo-Pacific plate during the early Cretaceous: Constraint from adakitic rocks in the Shaxi porphyry Cu–Au deposit, Lower Yangtze River Belt. *Lithos* **2016**, *262*, 651–667. [CrossRef]

69. Wang, Q.; Zhao, Z.H.; Xiong, X.L.; Xu, J.F. Melting of the underplated basaltic lower crust: Evidence from the Shaxi adakitic sodic quartz diorite-porphyrites, Anhui province, China. *Geochimica* **2001**, *30*, 353–362. (In Chinese)

70. Wang, Q.; Wyman, D.A.; Xu, J.F.; Zhao, Z.H.; Jian, P.; Xiong, X.L.; Bao, Z.W.; Li, C.F.; Bai, Z.H. Petrogenesis of Cretaceous adakitic and shoshonitic igneous rocks in the Luzong area, Anhui Province (eastern China): Implications for geodynamics and Cu-Au mineralization. *Lithos* **2006**, *89*, 424–446. [CrossRef]

71. Dilles, J.H.; Kent, A.J.R.; Wooden, J.L.; Tosdal, R.M.; Koleszar, A.; Lee, R.G.; Farmer, L.P. Zircon compositional evidence for sulfur-degassing from ore-forming arc magmas. *Econ. Geol.* **2015**, *110*, 241–251. [CrossRef]

72. Hou, T.; Charlier, B.; Holtz, F.; Veksler, I.; Zhang, Z.; Thomas, R.; Namur, O. Immiscible hydrous Fe-Ca-P melt and the origin of iron oxide-apatite ore deposits. *Nat. Commun.* **2018**, *9*, 1415. [CrossRef]

73. Hou, T.; Zhang, Z.C.; Kusky, T. Gushan magnetite–apatite deposit in the Ningwu basin, Lower Yangtze River Valley, SE China: Hydrothermal or Kiruna-type? *Ore Geol. Rev.* **2011**, *43*, 333–346. [CrossRef]

74. Fan, Y.; Dong, H.; Liu, Y.N.; Zhang, L.J. LA-ICP-MS titanite U-Pb dating and its signification in the Luohe iron deposit in the Lu-Zong volcanic basin. *Acta Petrol. Sin.* **2017**, *33*, 3395–3410. (In Chinese)

75. Claiborne, L.L.; Miller, C.F.; Wooden, J.L. Trace element composition of igneous zircon: A thermal and compositional record of the accumulation and evolution of a large silicic batholith, Spirit Mountain, Nevada. *Contrib. Mineral. Petrol.* **2010**, *160*, 511–531. [CrossRef]

76. Deering, C.D.; Keller, B.; Schoene, B.; Bachmann, O.; Beane, R.; Ovtcharova, M. Zircon record of the plutonic-volcanic connection and protracted rhyolite melt evolution. *Geology* **2016**, *44*, 267–270. [CrossRef]

77. Richards, J.P. High Sr/Y arc magmas and porphyry Cu ± Mo ± Au deposits: Just add water. *Econ. Geol.* **2011**, *106*, 1075–1081. [CrossRef]

78. Yu, J.J.; Chen, Y.C.; Mao, J.W.; Pirajno, F.; Duan, C. Review of geology, alteration and origin of iron oxide–apatite deposits in the Cretaceous Ningwu basin, Lower Yangtze River Valley, eastern China: Implications for ore genesis and geodynamic setting. *Ore Geol. Rev.* **2011**, *43*, 170–181. [CrossRef]

79. Yu, J.J.; Lu, B.C.; Wang, T.Z.; Che, L.R. Cretaceous Cu-Au, pyrite, and Fe-oxide-apatite deposits in the Ningwu basin, Lower Yangtze Area, Eastern China. *J. Asian Earth Sci.* **2015**, *103*, 150–168. [CrossRef]

80. Tarkian, M.; Koopmann, G. Platinum-group minerals in the Santo Tomas II (Philex) porphyry copper-gold deposit, Luzon Island, Philippines. *Miner. Depos.* **1995**, *30*, 39–47. [CrossRef]

81. Liang, Y.B.; Li, Y. Genetic types and geological characteristics of platinum group element deposits in China. *Miner. Resour. Geol.* **1997**, *11*, 145–151. (In Chinese)

82. Economou-Eliopoulos, M. *Platinum Group Element Potential of Porphyry Deposits*; Mineralogical Association of Canada: Québec City, QC, Canada, 2005; pp. 203–246.